

Resonant inelastic x-ray scattering in layered trimer iridate $\text{Ba}_4\text{NbIr}_3\text{O}_{12}$: the density functional approach

D.A. Kukusta,¹ L.V. Bekenov,¹ and V.N. Antonov¹

¹*G. V. Kurdyumov Institute for Metal Physics of the N.A.S. of Ukraine,
36 Academician Vernadsky Boulevard, UA-03142 Kyiv, Ukraine*

(Dated: March 3, 2026)

We have investigated the electronic structure of $\text{Ba}_4\text{NbIr}_3\text{O}_{12}$ within the density-functional theory (DFT) using the generalized gradient approximation while considering strong Coulomb correlations (GGA+ U) in the framework of the fully relativistic spin-polarized Dirac linear muffin-tin orbital band-structure method. $\text{Ba}_4\text{NbIr}_3\text{O}_{12}$ has a quasi-2D structure composed of corner-connected Ir_3O_{12} trimers containing three distorted face-sharing IrO_6 octahedra. The Ir atoms are distributed over two symmetrically inequivalent sites: the center of the trimer (Ir_1) and its two tips (Ir_2). The $\text{Ir}_1 - \text{Ir}_2$ distance within the trimer is quite small and equals to 2.547\AA at low temperature. As a result, there is clear formation of bonding and antibonding states. The large bonding-antibonding splitting stabilizes the d_{3z^2-1} -orbital-dominant antibonding state of $5d$ holes and produces a wide energy gap at the Fermi level. The ground state of $\text{Ba}_4\text{NbIr}_3\text{O}_{12}$ is a nonmagnetic singlet. Relatively moderate spin-orbit coupling (SOC) together with molecular orbital-like states in $\text{Ba}_4\text{NbIr}_3\text{O}_{12}$ suggest that the pure $J_{\text{eff}} = 1/2$ model may not be appropriate for this oxide. We have theoretically calculated the x-ray absorption spectroscopy (XAS) spectra at the Ir $L_{2,3}$ and Nb L_3 edges as well as the photoemission spectrum of $\text{Ba}_4\text{NbIr}_3\text{O}_{12}$. We have also presented a comprehensive investigation of the resonant inelastic x-ray scattering (RIXS) spectra at the Ir L_3 , O K , Nb K , L_3 , M_3 , M_5 , and N_3 edges. The RIXS spectrum of $\text{Ba}_4\text{NbIr}_3\text{O}_{12}$ at the Ir L_3 edge possesses several sharp features ≤ 2 eV corresponding to transitions within the Ir t_{2g} levels. The peak located at ~ 3.2 eV is found to be due to $t_{2g} \rightarrow e_g$ transitions. Some amount of $t_{2g} \rightarrow t_{2g}$ transitions also contribute to the intensity of this peak. The high energy fine structure ≥ 5.3 eV is mostly determined by $5d_{\text{O}} \rightarrow t_{2g}$ and $\text{O}_{2p} \rightarrow e_g$ transitions. The spectral features between 8 and 12 eV are due to $5d_{\text{O}} \rightarrow e_g$ transitions. We have also presented the investigation of the dependence of the Ir L_3 RIXS spectrum on the momentum transfer vector \mathbf{Q} and incident photon energy E_i .

PACS numbers: 75.50.Cc, 71.20.Lp, 71.15.Rf

I. INTRODUCTION

The interplay between orbital, spin, charge carriers, and lattice degrees of freedom has been a fascinating subject for the condensed-matter physics community for the last few decades. The $5d$ transition-metal compounds possess the same order of magnitude of on-site Coulomb repulsion U , spin-orbit coupling (SOC), and crystal-field energy [1]. So far, most researches have largely focused on iridium oxides for novel phenomena, such as topological insulators [2–5], Mott insulators [6–9], Weyl semimetals [10–12], and quantum spin liquids (QSLs) [13–15]. In a QSL, spins are strongly correlated, but quantum fluctuations prevent them from long-range ordering [15].

The specific physical properties of iridates strongly depend on local geometry. The most widely discussed geometry is the one with MO_6 octahedra (M is a transition-metal ion) sharing a common oxygen (a common corner) or two common oxygens (octahedra with a common edge). The first case takes place, for example, in the LaMnO_3 perovskite or the layered system La_2CuO_4 . The situation with a common edge occurs in many layered systems with triangular lattices such as NaCoO_2 and LiNiO_2 . The features of SO systems in both these cases were studied in detail (see, e.g., Ref. [16]). However, there exists yet the third typical geometry, which is also very often met in many real materials: the case of octahe-

dra with a common face (three common oxygens). This case has relatively small attention in the literature. Actually, there are many transition-metal compounds with the face-sharing geometry [17]. Such materials include, for example, the series of the 6H-hexagonal perovskite iridates $\text{Ba}_3\text{M}\text{Ir}_2\text{O}_9$ (M = Y^{3+} , Sc^{3+} , In^{3+} , Lu^{3+}) [18, 19]. These systems possess blocks of two face-sharing IrO_6 octahedra separated by MO_6 octahedra (which have common corners with IrO_6). They have two equivalent Ir sites, therefore, the oxidation state of Ir is fractional: $\text{Ba}_3\text{M}^{3+}\text{Ir}_2^{4.5+}\text{O}_9$. These systems have been extensively studied for novel quantum magnetic phases [20–30].

Another example with two blocks of face-sharing octahedra is the $\text{Ba}_5\text{AlIr}_2\text{O}_{11}$ barium oxide. The crystal structure of this compound consists of AlO_4 tetrahedra and IrO_6 octahedra. The latter share a face and develop Ir_2O_9 dimers, which spread along the a axis. Therefore, the compound would become geometrically frustrated in the presence of antiferromagnetic (AFM) interaction. Novel properties are expected from this structural arrangement in addition to those driven by SOC. Opposite to the $\text{Ba}_3\text{M}\text{Ir}_2\text{O}_9$ systems, $\text{Ba}_5\text{AlIr}_2\text{O}_{11}$ features dimer chains of two inequivalent octahedra occupied by tetravalent Ir^{4+} ($5d^5$) and pentavalent Ir^{5+} ($5d^4$) ions, respectively. $\text{Ba}_5\text{AlIr}_2\text{O}_{11}$ is a Mott insulator that undergoes a subtle structural phase transition near $T_S = 210$ K and a transition to magnetic order at $T_M = 4.5$ K.

Recently, unconventional electronic and magnetic ground states have been reported in compounds with Ir trimers, i.e., three face-sharing IrO_6 octahedra, which are much less explored so far [31–33]. Among them, $\text{Ba}_4\text{Ir}_3\text{O}_{10}$ with a Ir $5d^5$ nominal atomic configuration and a monoclinic $P2_1/a$ structure [34]. There are several experimental investigations of the physical properties of $\text{Ba}_4\text{Ir}_3\text{O}_{10}$ with some controversial results and conclusions [17, 33–39].

Here we report a theoretical investigation of the electronic structure of the $\text{Ba}_4\text{NbIr}_3\text{O}_{12}$ oxide. This perovskite belongs to the family of trimer-based $12L$ -hexagonal quadrupole perovskite counterparts with the general formula $\text{Ba}_4\text{MM}'_3\text{O}_{12}$ ($M = 3d$ transition metal or rare earth; $M' =$ heavier transition metal Ir, Rh, Ru, etc.). Their structures comprise single MO_6 octahedra and $\text{M}'_3\text{O}_{12}$ trimers of three face-sharing $\text{M}'\text{O}_6$ octahedra. These perovskites have received more limited attention, despite their potential to harbor novel quantum magnetism including QSL phases [40]. Most previous studies of $\text{Ba}_4\text{MM}'_3\text{O}_{12}$ perovskites focused on their structure and bulk magnetic properties [41, 42].

The Ir atoms in $\text{Ba}_4\text{NbIr}_3\text{O}_{12}$ are distributed over two symmetrically inequivalent sites: the center of the trimer (Ir_1) and its two tips (Ir_2). The shortest Ir-Ir bond is the one between Ir_1 and Ir_2 within the trimer. It has a length of $\sim 2.547 \text{ \AA}$ [33, 43], which is shorter than in the metallic iridium ($\sim 2.71 \text{ \AA}$ [44]) as well as in the dimer perovskites $\text{Ba}_5\text{AlIr}_2\text{O}_{11}$ ($\sim 2.73 \text{ \AA}$ [45]) and $\text{Ba}_3\text{InIr}_2\text{O}_9$ ($\sim 2.65 \text{ \AA}$ [26]), and the trimer oxide $\text{Ba}_4\text{Ir}_3\text{O}_{10}$ ($\sim 2.58 \text{ \AA}$ [34]).

Recently, Nguyen *et al.* investigated three trimer systems $\text{Ba}_4\text{NbM}'_3\text{O}_{12}$ ($M' = \text{Ir, Rh, Ru}$) as candidate QSL materials [32, 46]. Thakur *et al.* investigated the magnetic structure of $\text{Ba}_4\text{Nb}_{0.8}\text{Ir}_{3.2}\text{O}_{12}$ single crystals also to reveal the possibility of a spin-liquid state [47]. Bandyopadhyay *et al.* investigated experimentally the magnetic ground state in $\text{Ba}_4\text{NbIr}_3\text{O}_{12}$ [40] using a diverse range of techniques including powder x-ray diffraction (XRD), x-ray absorption spectroscopy (XAS) and x-ray photoemission spectroscopies (XPES), electrical resistivity, dc and ac magnetic susceptibilities, specific heat, and muon spin rotation/relaxation (μSR). The electrical resistivity together with XPS spectroscopy data as well as *ab initio* electronic structure calculations suggested an insulating electronic ground state of $\text{Ba}_4\text{NbIr}_3\text{O}_{12}$. The activated energy gap of $\sim 0.22\text{--}0.25 \text{ eV}$ was estimated from the temperature dependence of the electrical resistivity [40]. A quantitative analysis of Ir- $L_{2,3}$ XAS spectra established a moderate effective SOC strength for Ir [40]. The Curie-Weiss temperature for $\text{Ba}_4\text{NbIr}_3\text{O}_{12}$ is -13 K signaling rather small intercluster exchange [32]. $\text{Ba}_4\text{NbIr}_3\text{O}_{12}$ remains nonmagnetic down to the lowest temperatures and was suggested to be a spin liquid [32, 40, 48].

In this paper, we report a theoretical investigation from the first principles of the RIXS spectra of $\text{Ba}_4\text{NbIr}_3\text{O}_{12}$. The RIXS method has shown remarkable progress as a spectroscopic technique to record the mo-

mentum and energy dependence of inelastically scattered photons in complex materials. RIXS rapidly became the forefront of experimental photon science [49, 50]. RIXS combines spectroscopy and inelastic scattering to probe the electronic structure of materials. This method is also bulk sensitive, polarization dependent, as well as element and orbital specific [49]. It permits direct measurements of phonons, plasmons, single-magnons and orbitons, as well as other many-body excitations in strongly correlated systems, such as cuprates, nickelates, osmates, ruthenates, and iridates, with complex low-energy physics and exotic phenomena in the energy and momentum space.

Recently, the RIXS measurements at the Ir L_3 edge in $\text{Ba}_4\text{NbIr}_3\text{O}_{12}$ have been successfully performed by Magnaterra *et al.* [51] in the energy range up to 8.5 eV . In addition to the elastic peak centered at zero energy loss, the spectrum consists of several peaks below 2 eV and a peak at 3.8 eV . The authors also presented the dependence of the RIXS spectra on the momentum transfer vector \mathbf{Q} in the energy interval $\leq 2.5 \text{ eV}$.

Our detailed study of the electronic structure and RIXS spectra of $\text{Ba}_4\text{NbIr}_3\text{O}_{12}$ is carried out in terms of the density functional theory. The study sheds light on the important role of band structure effects and transition metal $5d -$ oxygen $2p$ hybridization in the spectral properties of $5d$ oxides. We use the *ab initio* approach using the fully relativistic spin-polarized Dirac linear muffin-tin orbital band-structure method. The paper is organized as follows. The crystal structure of $\text{Ba}_4\text{NbIr}_3\text{O}_{12}$ and computational details are presented in Sec. II. Section III presents the electronic structure of $\text{Ba}_4\text{NbIr}_3\text{O}_{12}$. In Sec. IV, the theoretical investigation of the Ir photoemission spectrum and XAS spectra at the Ir $L_{2,3}$ and Nb L_3 edges are presented. We also investigate theoretically the RIXS spectra of $\text{Ba}_4\text{NbIr}_3\text{O}_{12}$ at the Ir L_3 , O K , and Nb K , L_3 , M_3 , M_5 , and N_3 edges. The theoretical results are compared with experimental measurements. Finally, the results are summarized in Sec. V.

II. COMPUTATIONAL DETAILS

A. RIXS

In the direct RIXS process [49] the incoming photon with energy $\hbar\omega_{\mathbf{k}}$, momentum $\hbar\mathbf{k}$, and polarization $\boldsymbol{\epsilon}$ excites the solid from ground state $|g\rangle$ with energy E_g to intermediate state $|I\rangle$ with energy E_I . During relaxation an outgoing photon with energy $\hbar\omega_{\mathbf{k}'}$, momentum $\hbar\mathbf{k}'$ and polarization $\boldsymbol{\epsilon}'$ is emitted, and the solid is in state $|f\rangle$ with energy E_f . As a result, an excitation with energy $\hbar\omega = \hbar\omega_{\mathbf{k}} - \hbar\omega_{\mathbf{k}'}$ and momentum $\hbar\mathbf{q} = \hbar\mathbf{k} - \hbar\mathbf{k}'$ is created. Our implementation of the code for the calculation of the RIXS intensity uses Dirac four-component basis functions [52] in the perturbative approach [53]. RIXS is a second-order process, and its intensity is given by

TABLE I. The Wyckoff positions (WP) of $\text{Ba}_4\text{NbIr}_3\text{O}_{12}$ for the rhombohedral $R\bar{3}m$ (No. 166) crystal structure (lattice constants $a = 5.7827 \text{ \AA}$ and $c = 28.7725 \text{ \AA}$ [32]).

Structure	WP	Atom	x	y	z
$R\bar{3}m$ Ref. [32]	6c	Ba ₁	0	0	0.12890
	6c	Ba ₂	0	0	0.28585
	3a	Nb	0	0	0
	3b	Ir ₁	0	0	0.5
	6c	Ir ₂	0	0	0.41148
	18h	O ₁	0.48170	0.518309	0.12160
18h	O ₂	0.51460	0.48540	0.29560	

$$I(\omega, \mathbf{k}, \mathbf{k}', \epsilon, \epsilon') \propto \sum_{\mathbf{f}} \left| \sum_{\mathbf{I}} \frac{\langle \mathbf{f} | \hat{H}'_{\mathbf{k}'\epsilon'} | \mathbf{I} \rangle \langle \mathbf{I} | \hat{H}'_{\mathbf{k}\epsilon} | \mathbf{g} \rangle}{E_{\mathbf{g}} - E_{\mathbf{I}}} \right|^2 \times \delta(E_{\mathbf{f}} - E_{\mathbf{g}} - \hbar\omega), \quad (1)$$

where the RIXS perturbation operator in the dipole approximation is given by the lattice sum $\hat{H}'_{\mathbf{k}\epsilon} = \sum_{\mathbf{R}} \hat{\alpha}\epsilon \exp(-i\mathbf{k}\mathbf{R})$, where $\hat{\alpha}$ are the Dirac matrices. The sum over intermediate states $|\mathbf{I}\rangle$ includes the contributions from different spin-split core states at the given absorption edge. The matrix elements of the RIXS process in the frame of the fully relativistic Dirac LMTO method are presented in Ref. [54].

B. Crystal structure

The $\text{Ba}_4\text{NbIr}_3\text{O}_{12}$ compound was synthesized recently by L. T. Nguyen and R. J. Cava. [32]. The lattice and structural parameters are summarized in Table 1. The structure consists of three IrO_6 octahedra connected by face sharing to form Ir_3O_{12} trimers (Fig. 1). The trimers are arranged in a triangular planar lattice. While $\text{Ba}_4\text{LnIr}_3\text{O}_{12}$ (Ln = lanthanides) has the monoclinic $C2/m$ space group, $\text{Ba}_4\text{NbIr}_3\text{O}_{12}$ adopts a higher-symmetry rhombohedral $R\bar{3}m$ (No. 166) crystal structure [32]. The individual Ir_3O_{12} trimers share corners with nonmagnetic NbO_6 octahedra, and not with other trimers. The NbO_6 octahedra and Ir_3O_{12} trimers alternate along the c axis to generate a 12-layer (i.e., three layers of four octahedra) hexagonal perovskite structure. The unit cell of $\text{Ba}_4\text{NbIr}_3\text{O}_{12}$ contains two inequivalent Ba sites, two inequivalent O sites, and two inequivalent Ir sites [32]. The two Ir sites, Ir₁ and Ir₂, are located in the middle and outer positions of the trimer, respectively. In each trimer the two outside octahedra around Ir₂ ions are strongly distorted. The middle octahedron around the Ir₁ ion is less distorted. The Ir₁-O₁ distances are equal to 1.96727 Å, while the Ir₂-O₁ and Ir₂-O₂ distances are equal to 1.93698 and 2.14923 Å, respectively. The length of the shortest Ir-Ir bond, which is the one between Ir₁ and Ir₂ within the trimers, equals to 2.54694 Å.

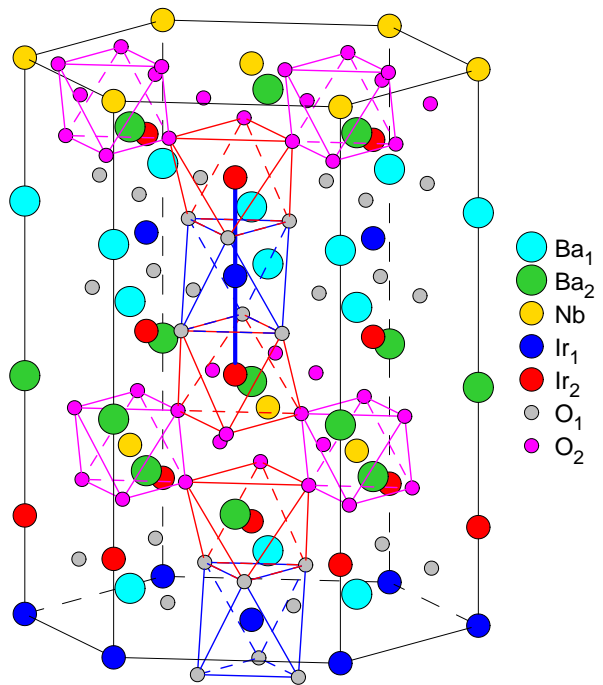


FIG. 1. (Color online) The schematic representation of $\text{Ba}_4\text{NbIr}_3\text{O}_{12}$ in the rhombohedral structure with the space group $R\bar{3}m$ (No. 166).

C. Calculation details

The details of the computational method are described in our previous papers [54–57] and here we only mention several aspects. The band structure calculations were performed using the fully relativistic LMTO method [58, 59]. This implementation of the LMTO method uses four-component basis functions constructed by solving the Dirac equation inside an atomic sphere [52]. The exchange-correlation functional of a GGA-type was used in the version of Perdew, Burke and Ernzerhof [60]. The Brillouin zone integration was performed using the improved tetrahedron method [61]. The basis consisted of Nb, Ir, and Ba s , p , d , and f ; and O s , p , and d LMTO's.

In the RIXS process, an electron is promoted from a core level to an intermediate state, leaving a core hole. As a result, the electronic structure of this state differs from that of the ground state. To reproduce the experimental spectrum, the self-consistent calculations should be carried out including a core hole. Usually, the core-hole effect has no impact on the shape of XAS at the $L_{2,3}$ edges of $5d$ systems [59]. However, the core hole has a strong effect on the RIXS spectra in transition metal compounds [54, 62]; therefore, we consider it in our calculations.

In our calculations, we rely on the experimentally measured atomic positions and lattice constants, because they are well established for this material and still more accurate than those obtained from DFT.

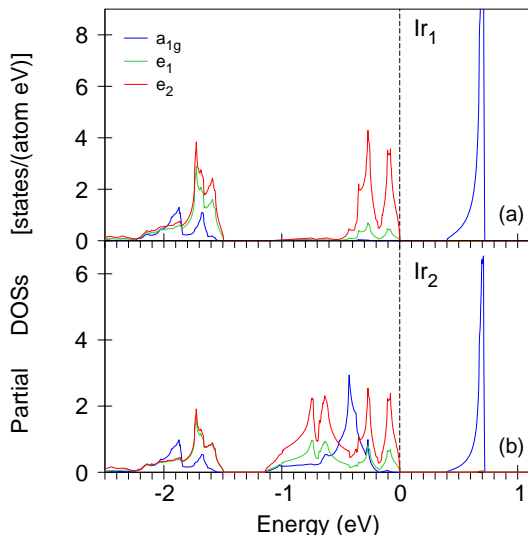


FIG. 2. (Color online) The orbital-resolved Ir t_{2g} partial density of states (DOS) [in states/(atom eV)] for $\text{Ba}_4\text{NbIr}_3\text{O}_{12}$ calculated in the GGA approach at the Ir₁ (a) and Ir₂ (b) sites.

III. ELECTRONIC STRUCTURE

We performed GGA, GGA+SO, and GGA+SO+ U calculations of the electronic structure of $\text{Ba}_4\text{NbIr}_3\text{O}_{12}$. The crystal field at the Ir site ($D3d$ and $C3v$ point symmetry for Ir₁ and Ir₂ sites, respectively) causes the splitting of $5d$ orbitals into one singlet a_{1g} (d_{3z^2-1}), and two doublets e_1 (d_{xz} and d_{yz}) and e_2 ($d_{x^2-y^2}$ and d_{xy}). The a_{1g} orbitals are oriented head-on in the face sharing geometry. In Fig. 2 the plots of orbital-resolved partial density of states (DOS) for $\text{Ba}_4\text{NbIr}_3\text{O}_{12}$ at the Ir₁ and Ir₂ sites calculated in the GGA approach are presented. Both the Ir₁ and Ir₂ ions possess strong empty DOS peaks at ~ 0.7 . There is an energy gap between the antibonding a_{1g} and e_2 states. The partial DOS is quite different for the two nonequivalent Ir sites.

Every Ir₁ ion has two neighboring Ir ions in its close vicinity at ~ 2.547 Å [32]. However, Ir₂ ions have only one neighboring Ir ion at the same distance in the trimer structure. As a result, the Ir₁ ions have a tendency of dimerization and of forming quasi-molecular orbital (QMO) states. The a_{1g} (d_{3z^2-1}) orbital provides the dominant character of the lowest (-1.9 eV) occupied subband and the highest ($+0.7$ eV) empty subband. These two subbands with predominant d_{3z^2-1} character can be assigned to the bonding and antibonding states of Ir₁ dimer molecules with a splitting energy of ~ 2.6 eV. The large bonding-antibonding splitting stabilizes the d_{3z^2-1} -orbital-dominant antibonding state and produces a wide energy gap at the Fermi level. The Ir₂ site also possesses the bonding and antibonding a_{1g} (d_{3z^2-1}) states at the same positions, but in addition there are non-bonding a_{1g} states at -0.4 eV [see Fig. 2(b)], which

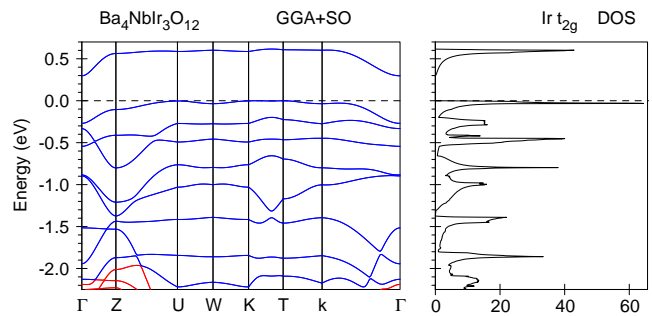


FIG. 3. (Color online) The energy band structure and total density of states (DOS) [in states/(cell eV)] for t_{2g} states in $\text{Ba}_4\text{NbIr}_3\text{O}_{12}$ calculated in the GGA+SO approach.

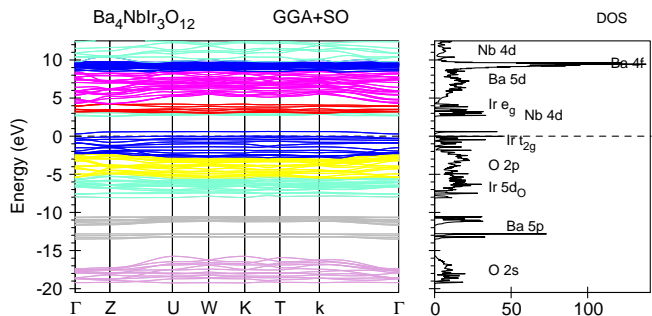


FIG. 4. (Color online) The energy band structure and total density of states (DOS) [in states/(cell eV)] for $\text{Ba}_4\text{NbIr}_3\text{O}_{12}$ calculated in the GGA+SO approach.

are absent for the Ir₁ site. It is important to note that the energy gap in $\text{Ba}_4\text{NbIr}_3\text{O}_{12}$ is already opened in the GGA or GGA+SO approaches without any Hubbard U . Besides, our self-consistent calculations always produce nonmagnetic (NM) solutions for $\text{Ba}_4\text{NbIr}_3\text{O}_{12}$. Even if we start from a magnetic spin-polarized situation, our calculations (in the GGA, GGA+SO and GGA+SO+ U approaches) converge to a nonmagnetic solution. It is in agreement with experimental observations, which claim that $\text{Ba}_4\text{NbIr}_3\text{O}_{12}$ remains nonmagnetic down to the lowest temperatures [48]. So, the ground state of $\text{Ba}_4\text{NbIr}_3\text{O}_{12}$ is just a nonmagnetic singlet and this oxide can be considered as a nonmagnetic noncorrelated band insulator. From this point of view, the absence of magnetic ordering in $\text{Ba}_4\text{NbIr}_3\text{O}_{12}$ could be not due to the spin-liquid state anticipated in Ref. [32, 40] but just due to the formation of such nonmagnetic QMO state.

In $\text{Ba}_4\text{NbIr}_3\text{O}_{12}$, the inter-trimer-couplings are very small, so the electrons are localized within the trimers, resulting in dielectric behavior. This is supported by the band structure shown in Fig. 3, where the Ir t_{2g} bands calculated in the GGA+SO approach are very narrow and avoid crossing one another. In other words, they look just like the energy levels of molecular orbitals.

Figures 4 and 5 present the energy band structure and partial DOSs, respectively, in $\text{Ba}_4\text{NbIr}_3\text{O}_{12}$ in the

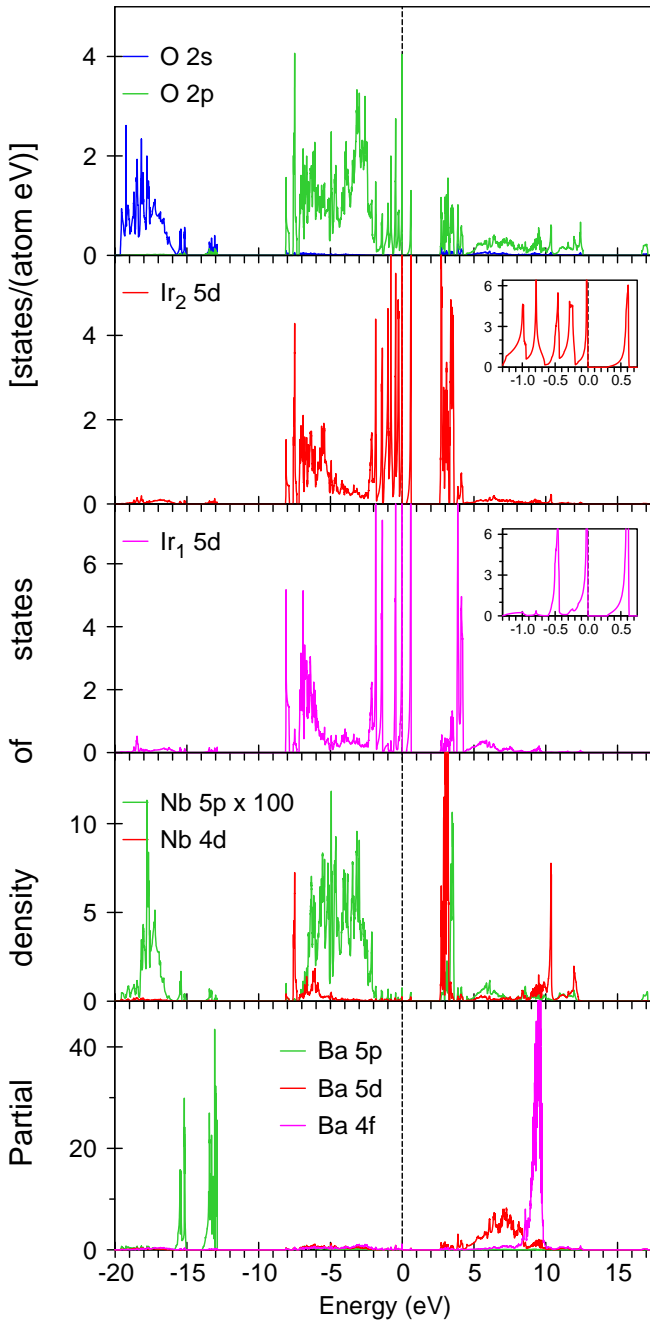


FIG. 5. (Color online) The partial density of states [in states/(atom eV)] for $\text{Ba}_4\text{NbIr}_3\text{O}_{12}$ calculated in the GGA+SO approach.

GGA+SO approach. The occupied t_{2g} states are situated in the energy interval from -0.85 eV to E_F . There is a significant amount of Ir $5d$ DOS located at the bottom of the oxygen $2p$ states from -7.1 to -5.2 eV below the Fermi energy. These so called Ir $5d_O$ states are provided by the tails of oxygen $2p$ states inside the Ir atomic spheres and play an essential role in the photo-emission spectrum as well as in the RIXS spectrum at the Ir L_3

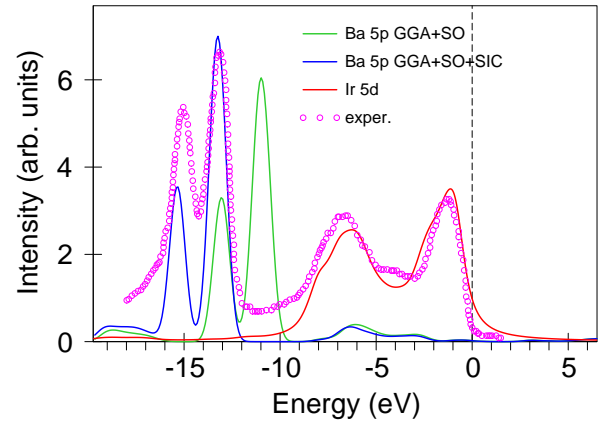


FIG. 6. (Color online) The experimentally measured by Bandyopadhyay *et al.* [40] valence band photoemission spectrum for $\text{Ba}_4\text{NbIr}_3\text{O}_{12}$ (open magenta circles) compared with the Ir $5d$ (the red curve) partial DOS calculated in the GGA+SO approach and Ba $5p$ quasi-core partial DOS calculated in the GGA+SO (the green curve) and GGA+SO+SIC (the blue curve) approaches. The partial DOSs have been multiplied by their photoionization cross sections.

edge (see Section IV). The occupied Nb $4d$ states possess a two-peak structure with a narrow peak at -7.5 eV and a wide peak from -6 to -5.7 eV. The empty Nb $4d$ states have a strong peak from 2.6 to 3.3 eV and two smaller peaks at 10.4 and 12 eV. It is interesting to note that the empty Nb $4d$ states are hybridized mostly with Ir₂ $5d$ states but not with Ir₁ $5d$ states because the intersite Nb–Ir₂ distance is much smaller than the corresponding Nb–Ir₁ distance (4.0252 Å and 5.8432 Å, respectively). The Nb $5p$ occupied states are well hybridized with oxygen $2s$ and $2p$ states from -18.2 to -16.1 eV and from -6.4 to -2 eV, respectively. The Ba $5d$ states occupy the energy region from 4.8 to 8.5 eV above the energy Fermi. A narrow and intensive DOS peak of Ba $4f$ states is located just above the Ba $5d$ states from 8.7 to 9.9 eV. The Ba $5p$ quasi-core level has two DOS peaks split by SOC corresponding to $5p_{1/2}$ and $5p_{3/2}$ states. There is small hybridization of Ba $5p$ states with Nb $5p$ and oxygen $2s$ states. The oxygen $2s$ states are situated far below the Fermi level from -19.6 to -15.2 eV. The occupied O $2p$ states are localized from -8.1 eV to E_F . They are strongly hybridized with Ir $5d$ states between -2.2 eV and E_F . The empty oxygen $2p$ states are strongly hybridized with Ir t_{2g} states just above the Fermi level and with Ir e_g states. They are also hybridized with Ba $5d$ and $4f$ states.

IV. PES, XAS, AND RIXS SPECTRA

A. Ir photoemission spectra

Figure 6 shows the experimentally measured by Bandyopadhyay *et al.* [40] valence band photoemission spectrum (PES) for $\text{Ba}_4\text{NbIr}_3\text{O}_{12}$ (open magenta circles) compared with the Ir $5d$ (the red curve) and Ba $5p$ quasi-core PDOS (the green curve) calculated in the GGA+SO approach. We obtain the PES spectrum from the PDOS by multiplying the PDOS by its photoionization cross section as well as the Fermi function, and then broadening the result of multiplication. The peak situated between -4 eV and E_F reflects the Ir t_{2g} states for both Ir₁ and Ir₂ ions. The next peak from -9 to -4 eV represents the energy distribution of the Ir $5d_O$ states provided by the tails of oxygen $2p$ states inside the Ir atomic spheres and situated at the bottom of the oxygen $2p$ states from -7.1 to -5.2 eV below the Fermi energy (see Fig. 5). Our GGA+SO calculations provide good agreement in the energy position and the relative intensity of these two high energy peaks. The two deep peaks in PES between -16.5 and -12 eV reflect the Ba $5p$ quasi-core level split by SOC into the $5p_{1/2}$ and $5p_{3/2}$ contributions. The GGA+SO approach was not able to reproduce the correct energy position of the Ba $5p$ quasi-core levels shifting them toward the Fermi level (the green curve in Fig. 6). A similar description was observed also in the theoretical calculations by Bandyopadhyay *et al.* [40] (see Fig. 4c in their publication). To reproduce the experimental energy position of the Ba $5p$ states we had to take into account strong correlations of the Ba $5p$ states. We used a self-interaction-like correction (SIC) procedure [63, 64], where the valence bands are shifted downwards by adding to the Hamiltonian a SIC-like orbital-dependent potential V_l . We used the value of $V_l = 2.5$ eV in our band structure calculations applied to the Ba $5p$ orbitals. The GGA+SO+SIC approach provides excellent agreement with the experiment (see the blue curve in Fig. 6). A similar method was used in the calculations of the energy band structure, optical and RIXS spectra in Ta_2NiSe_5 . To obtain a correct energy gap and experimental optical and RIXS spectra in this chalcogenide researchers applied V_l of the same value to the Se $4p$ states [65–67].

B. Ir and Nb $L_{2,3}$ XAS spectra

Figure 7 presents the experimentally measured [40] x-ray absorption spectra at the Ir $L_{2,3}$ edges in $\text{Ba}_4\text{NbIr}_3\text{O}_{12}$ in comparison with the ones theoretically calculated in the GGA+SO approach. There is good agreement between the calculated and experimental spectra. The isotropic XAS spectra are mostly dominated by empty e_g states with a smaller contribution from empty t_{2g} orbitals at lower energy.

The XAS spectra can provide a direct probe of SOC through a branching ratio $\text{BR} = I_{L_3}/I_{L_2}$. In the limit

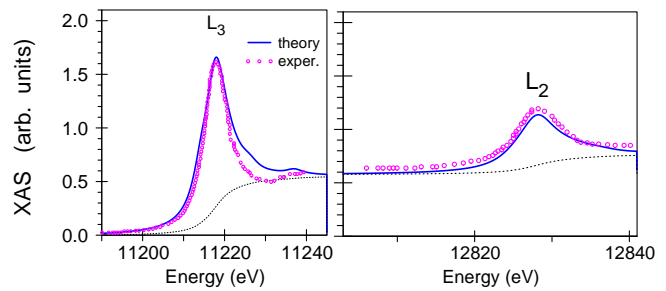


FIG. 7. (Color online) The experimentally measured by Bandyopadhyay *et al.* [40] x-ray absorption spectra at the Ir $L_{2,3}$ edges in $\text{Ba}_4\text{NbIr}_3\text{O}_{12}$ (open magenta circles) in comparison with the ones theoretically calculated in the GGA+SO approach. The dotted black curves show the background scattering intensity.

of negligible SOC effects, the statistical branching ratio $\text{BR} = 2$, and the L_3 white line is twice the size of the L_2 feature [68]. The theoretically calculated BR in $\text{Ba}_4\text{NbIr}_3\text{O}_{12}$ is equal to 2.72 for the Ir₁ site and 2.95 for the Ir₂ site. The branching ratio for the experimentally measured XAS spectra $\text{BR} \approx 3.11$ [40]. It is smaller than for strongly spin-orbit coupled iridates, such as Sr_2IrO_4 , for which theory gives $\text{BR} = 3.56$ [69] and experiment gives $\text{BR} = 4.1$ [70]. The combined effects of noncubic crystal distortion, Ir-O covalency, strong hybridization resulting from direct orbital overlap of neighboring Ir- $5d$ states, intersite Ir-Ir direct hopping, and a large bandwidth suppress the effective SOC strength on $\text{Ba}_4\text{NbIr}_3\text{O}_{12}$. Relatively moderate SOC together with molecular orbital-like states in $\text{Ba}_4\text{NbIr}_3\text{O}_{12}$ suggest that the pure $J_{\text{eff}} = 1/2$ model may not be appropriate for this oxide. It is better use a description based on molecular orbital-like states. There are several other examples in the literature of covalency-driven collapse of the $J_{\text{eff}} = 1/2$ model in dimer/trimer-based iridium oxide systems consisting of face-sharing Ir-O octahedra [71–74] as well as in the high pressure $\beta\text{-Li}_2\text{IrO}_3$ iridate [75–77].

Figure 8 presents the experimentally measured [40] x-ray absorption spectrum at the Nb L_3 edge in $\text{Ba}_4\text{NbIr}_3\text{O}_{12}$ (open magenta circles) in comparison with the one theoretically calculated in the GGA+SO approach. The spectrum is due to $2p_{3/2} \rightarrow 4d_{3,2,5/2}$ transitions and possesses two peaks. The low energy peak reflects the transitions from the core level into the strong narrow empty DOS peak situated at 2.6–3.3 eV. The high energy peak is due to the transitions into the two smaller DOS peaks at 10.4 and 12 eV (see Fig. 5). The theory reproduces well the relative intensities of these two peaks but shifts the second peak towards higher energy.

C. Ir, O, and Nb RIXS spectra

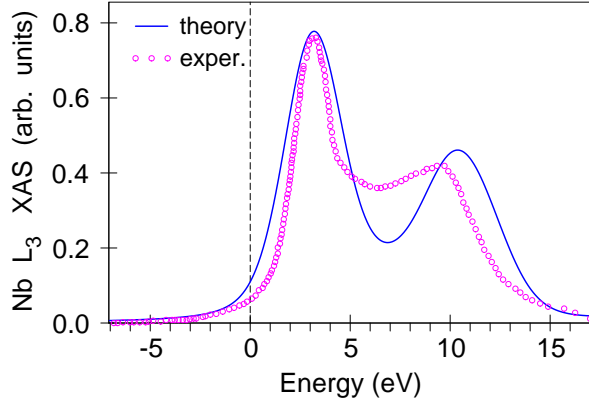


FIG. 8. (Color online) The experimentally measured by Bandyopadhyay *et al.* [40] x-ray absorption spectrum at the Nb L_3 edge in $\text{Ba}_4\text{NbIr}_3\text{O}_{12}$ (open magenta circles) in comparison with the one theoretically calculated in the GGA+SO approach.

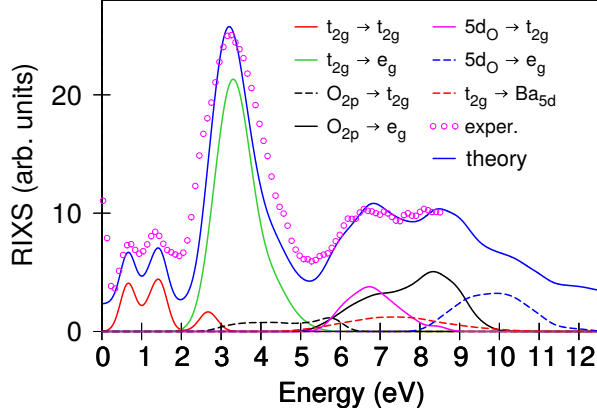


FIG. 9. (Color online) The experimental resonant inelastic x-ray scattering (RIXS) spectrum (open magenta circles) measured by Magnaterra *et al.* [51] at the Ir L_3 edge at 300 K for incident energy of 11215 eV and the momentum transfer vector $\mathbf{Q} = (0.7, 0, 36.7)$ in reciprocal lattice units (r.l.u.) for the rhombohedral $R\bar{3}m$ crystal structure of $\text{Ba}_4\text{NbIr}_3\text{O}_{12}$ compared with the one theoretically calculated in the GGA+SO approach for the same incident energy and momentum transfer vector \mathbf{Q} . Calculated partial contributions from different interband transitions are also presented.

a. Ir L_3 RIXS spectrum The experimental RIXS spectrum at the Ir L_3 edge was measured by Magnaterra *et al.* [51] in the energy range up to 8.5 eV. In addition to the elastic peak centered at zero energy loss, the spectrum consists of two peaks below 2 eV, a strong peak at 3.2 eV, and a wide fine structure ≥ 5.3 eV. Figure 9 presents the theoretically calculated (the full blue curve) and experimentally measured (open magenta circles) RIXS spectra at the Ir L_3 edge for $\text{Ba}_4\text{NbIr}_3\text{O}_{12}$ [51]. We also present calculated partial contributions from different transitions between the energy bands. We

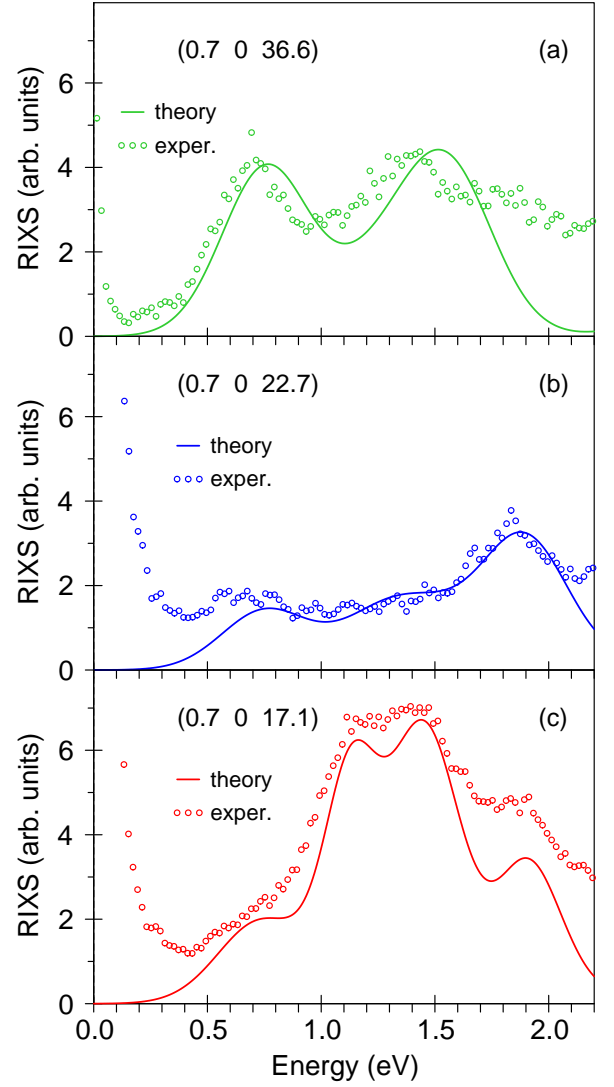


FIG. 10. (Color online) The experimental resonance inelastic x-ray scattering (RIXS) spectra (open magenta circles) measured by Magnaterra *et al.* [51] at the Ir L_3 edge at 300 K for the momentum transfer vector $\mathbf{Q} = (0.7, 0, Q_z)$ for selected values of Q_z in reciprocal lattice units (r.l.u.) compared with the ones theoretically calculated in the GGA+SO approach.

found that the fine structure situated below 2 eV corresponds to intra- t_{2g} excitation (the red curve in Fig. 9). The peak located at ~ 3.2 eV was found to be due to $t_{2g} \rightarrow e_g$ transitions (the green curve). Some amount of $t_{2g} \rightarrow t_{2g}$ transitions also contribute to the intensity of this peak. The two peak high energy fine structure ≥ 5.3 eV is mostly determined by $5d_O \rightarrow t_{2g}$ (the magenta curve) and $O_{2p} \rightarrow e_g$ (the black curve) transitions. The transitions $O_{2p} \rightarrow t_{2g}$ (the dashed black curve) and $t_{2g} \rightarrow \text{Ba}_{5d}$ (the dashed red curve) are relatively weak. The spectral features between 8 and 12 eV are due to $5d_O \rightarrow e_g$ transitions (the dashed blue curve).

It is widely believed that $d-d$ excitations show only

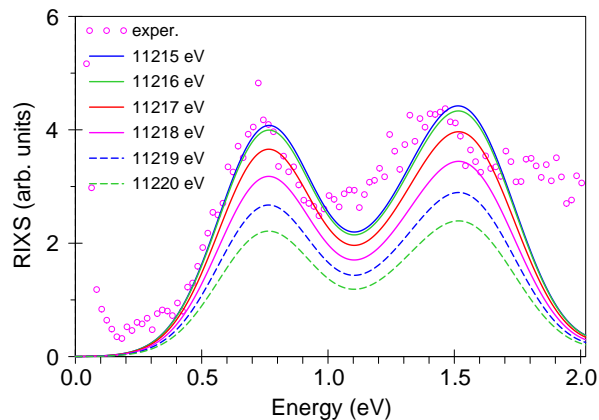


FIG. 11. (Color online) The theoretically calculated resonant inelastic x-ray scattering (RIXS) spectra at the Ir L_3 edge in $\text{Ba}_4\text{NbIr}_3\text{O}_{12}$ for the momentum transfer vector $\mathbf{Q} = (0.7, 0, 36.6)$ in reciprocal lattice units as a function of incident photon energy E_i .

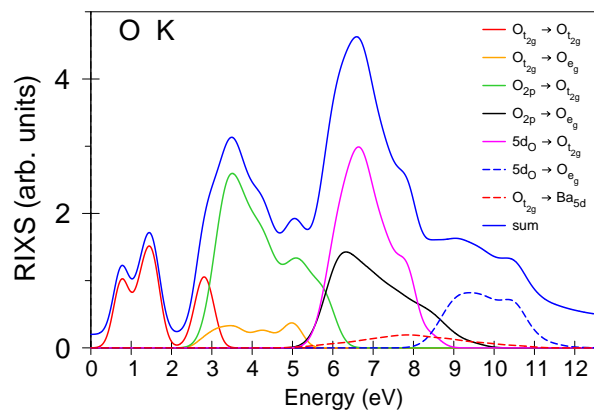


FIG. 12. (Color online) The theoretically calculated resonant inelastic x-ray scattering (RIXS) spectrum at the O K edge in $\text{Ba}_4\text{NbIr}_3\text{O}_{12}$ and partial contributions from different interband transitions.

small momentum transfer vector \mathbf{Q} dependence in $5d$ transition metal compounds [78, 79]. Figure 10 shows the experimental resonant inelastic x-ray scattering (RIXS) spectra (open circles) measured by Magnaterra *et al.* [51] at the Ir L_3 edge at 300 K for the transferred momentum $\mathbf{Q} = (0.7, 0, Q_z)$ parallel to the trimer axis for selected values of Q_z in reciprocal lattice units (r.l.u.) compared with the ones theoretically calculated in the GGA+SO approach. There is relatively large \mathbf{Q} dependence of the RIXS spectrum at the Ir L_3 edge with pronounced periodic modulation of the RIXS intensity as a function of Q_z . This provides additional evidence for the quasi-molecular character of the electronic structure of $\text{Ba}_4\text{NbIr}_3\text{O}_{12}$ [51, 74, 80, 81]. The theory describes quite well the dependence of the RIXS spectrum on Q_z . The high energy fine structures >2.5 eV are changed insignif-

icantly with Q_z .

Figure 11 shows the Ir L_3 RIXS spectrum for the momentum transfer vector $\mathbf{Q} = (0.7, 0, 36.6)$ as a function of incident photon energy E_i above the corresponding edge. We found that the low energy fine structure corresponding to intra- t_{2g} excitations steadily decreases when the incident photon energy changes from 11215 to 11220 eV.

b. O K RIXS spectrum Figure 12 shows the theoretically calculated RIXS spectrum at the O K edge in $\text{Ba}_4\text{NbIr}_3\text{O}_{12}$ in the GGA+SO approach together with the partial contributions from different transitions between the energy bands. The shape of the oxygen K RIXS spectrum at 0–5 eV is very similar to the corresponding RIXS spectrum at the Ir L_3 edge. The two peaks at ≤ 2 eV are derived from $O_{t_{2g}} \rightarrow O_{t_{2g}}$ transitions (the red curve): the interband transitions between the oxygen $2p$ states strongly hybridized with the Ir t_{2g} states in close vicinity to the Fermi level. At the same time, $O_{t_{2g}} \rightarrow O_{e_g}$ transitions are very weak (the orange curve). We found that the major contribution to the fine structure situated from 2 to 5 eV is derived from $O_{2p} \rightarrow O_{t_{2g}}$ transitions (the green curve), while $O_{2p} \rightarrow O_{e_g}$ transitions are less intensive (the black curve). Opposite to the Ir L_3 RIXS spectrum, the intensity of the oxygen K RIXS spectrum for energies ≥ 5 eV is very large. These structures are derived from $5d_O \rightarrow O_{t_{2g}}$ (the magenta curve), $O_{2p} \rightarrow O_{e_g}$ (the black curve), and $O_{t_{2g}} \rightarrow \text{Ba}_{5d}$ transitions. Experimental measurements of the RIXS spectrum at the O K edge in $\text{Ba}_4\text{NbIr}_3\text{O}_{12}$ are highly desirable.

c. Nb RIXS spectra At the core level RIXS is not only element-specific but also orbital specific. For $3d$ transition metals, the electronic states can be probed by K , $L_{2,3}$ and $M_{2,3}$ x-ray absorption, emission, and RIXS spectra. For $4d$ transition metals, the electronic states can be probed by K , $L_{2,3}$, $M_{2,3}$, $M_{4,5}$, and $N_{2,3}$ spectra, whereas in $5d$ transition metals one can also use extra $N_{4,5}$, $N_{6,7}$, and $O_{2,3}$ spectra. For unpolarized absorption spectra, transitions with $\Delta l = \pm 1, \Delta j = 0, \pm 1$ (one-particle dipole selection rules) are allowed only. Therefore, only electronic states with appropriate symmetry contribute to the absorption, emission, and RIXS spectra under consideration (Table II). To investigate the influence of the core state on the resulting Nb RIXS spectra in $\text{Ba}_4\text{NbIr}_3\text{O}_{12}$ we calculated the RIXS spectra at the Nb K , L_3 , M_3 , M_5 , and N_3 edges. The results are presented in Fig. 13.

Figures 13(a) and 13(b) show the RIXS spectra at the Nb K and M_5 edges calculated in the GGA+SO approach. The exchange splitting of the initial $1s$ core state is extremely small [59, 82], therefore only the exchange and spin-orbit splitting of the $5p$ states is responsible for the observed RIXS spectrum at the Nb K edge. The Nb K RIXS spectrum consists of two major peaks at 5.6 and 8.6 eV energy. The low energy peak is due to the interband transitions from the occupied Nb $5p$ states hybridized with oxygen $2p$ states to the empty Nb $5p$ states

TABLE II. Angular momentum symmetry levels indicating the dipole allowed transitions from core states to the unoccupied valence states in transition metals with the partial density of states character.

Spectra	L_2		L_3		M_4	M_5	N_6	N_7
	K	M_2	M_3	N_2				
		O_2	O_3					
Core level	$1s_{1/2}$	$2p_{1/2}$	$2p_{3/2}$	$3d_{3/2}$	$3d_{5/2}$	$4f_{5/2}$	$4f_{7/2}$	
		$4p_{1/2}$	$4p_{3/2}$	$4d_{3/2}$	$4d_{5/2}$			
		$5p_{1/2}$	$5p_{3/2}$					
Valence states	$p_{1/2}$	$s_{1/2}$	$s_{1/2}$	$p_{1/2}$	$p_{3/2}$	$d_{3/2}$	$d_{5/2}$	
	$p_{3/2}$	$d_{3/2}$	$d_{3/2}$	$p_{3/2}$	$f_{5/2}$	$d_{5/2}$	$g_{7/2}$	
	-	-	$d_{5/2}$	$f_{5/2}$	$f_{7/2}$	$g_{7/2}$	$g_{9/2}$	

hybridized with Ir t_{2g} and e_g states. The high energy peak is due the transitions between Nb $5p$ states and the states derived from the hybridization with Ba $5d$ states.

The Nb M_5 spectrum can be to some extent considered as an analog of the K spectrum. The Nb K RIXS spectrum reflects the energy distribution of $5p_{1/2}$ and $5p_{3/2}$ energy states (Table II). The M_5 RIXS spectrum due to the dipole selection rules occurs for the transitions from the $3d_{3/2}$ core state to $5p_{3/2}$, $4f_{5/2}$, and $4f_{7/2}$ states. Comparing this spectrum with the corresponding Nb K RIXS spectrum one can see an obvious resemblance between them. The major difference is seen from 0 to 7 eV. The difference between the Nb K and M_5 spectra can be attributed to an additional contribution of $4f_{5/2,7/2}$ energy states to the M_5 spectrum as well as to the difference in the radial matrix elements ($1s \rightarrow 5p_{1/2,3/2}$ for the K spectrum and $3d_{5/2} \rightarrow 5p_{3/2}$ for the M_5 spectrum). Although the latter plays a minor role due to the fact that the radial matrix elements are smooth functions of energy [59].

The RIXS spectra in the row $L_3 - M_3 - N_3$ have almost a similar shape and demonstrate a systematic decrease of intensity [Figures 13(c,d,e)]. These spectra are more narrow than the K and M_5 RIXS spectra and shifted towards higher energy. This can be explained by a smaller width of occupied Nb $4d$ states in comparison with the corresponding Nb $5p$ states. Besides, Nb $4d$ states are situated below Nb $5p$ states in energy (see Fig. 5).

V. CONCLUSIONS

To summarize, we have investigated the electronic structure of $\text{Ba}_4\text{NbIr}_3\text{O}_{12}$ in the frame of the fully relativistic spin-polarized Dirac approach. We have also presented comprehensive theoretical calculations of the RIXS spectra at the Ir L_3 , oxygen K , Nb K , L_3 , M_3 , M_5 , and N_3 edges as well as the XAS spectra at the Ir $L_{2,3}$ and Nb L_3 edges. To investigate the occupied valence states we have calculated the photoemission spectrum in $\text{Ba}_4\text{NbIr}_3\text{O}_{12}$. The theoretically calculated spectra are

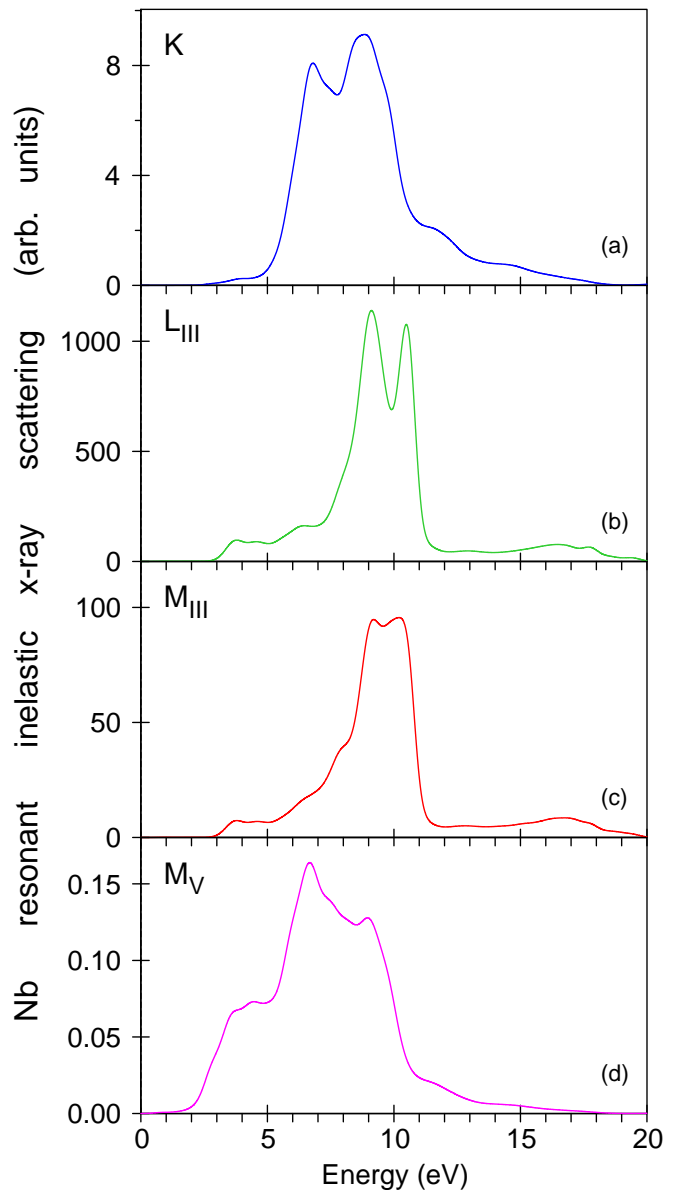


FIG. 13. (Color online) The theoretically calculated resonant inelastic x-ray scattering (RIXS) spectra at the Nb K (a), M_5 (b), L_3 (c), M_3 (d), and N_3 (e) edges in $\text{Ba}_4\text{NbIr}_3\text{O}_{12}$.

in good agreement with the experimental data.

$\text{Ba}_4\text{NbIr}_3\text{O}_{12}$ has a quasi-2D structure composed of corner-connected Ir_3O_{12} trimers containing three distorted face-sharing IrO_6 octahedra. The Ir atoms are distributed over two symmetrically inequivalent sites: at the center of the trimer (Ir_1) and its two tips (Ir_2). The $\text{Ir}_1 - \text{Ir}_2$ distance within the trimer is quite small and equals to 2.547 Å. As a result, there is clear formation of bonding and antibonding states. The large bonding-antibonding splitting stabilizes the d_{3z^2-1} -orbital-dominant antibonding state of $5d$ holes and produces a wide energy gap at the Fermi level. The Ir t_{2g} bands are found to split into distinct states with mixed character and these different

states avoid crossing one another, suggesting the formation of molecular orbital-like mixed orbitals within the Ir_3O_{12} trimers. Additional evidence of the QMO picture is that the ground state of $\text{Ba}_4\text{NbIr}_3\text{O}_{12}$ is a nonmagnetic singlet. The theoretically calculated BR in $\text{Ba}_4\text{NbIr}_3\text{O}_{12}$, which can be considered as a direct probe of SOC, is equal to 2.72 for the Ir_1 site and 2.95 for the Ir_2 site. It is smaller than for strongly spin-orbit coupled iridates, such as Sr_2IrO_4 . Relatively moderate SOC together with molecular orbital-like states in $\text{Ba}_4\text{NbIr}_3\text{O}_{12}$ suggest that the pure $J_{\text{eff}} = 1/2$ model may not be appropriate for this oxide. It is better use a description based on molecular orbital-like states.

The theoretically calculated Ir L_3 RIXS spectrum is in good agreement with the experiment. We found that the low energy part of the RIXS spectrum ≤ 2 eV corresponds to intra- t_{2g} excitations. The peak located at ~ 3.2 eV was found to be due to $t_{2g} \rightarrow e_g$ transitions. Some amount of $t_{2g} \rightarrow t_{2g}$ transitions also contribute to the intensity of this peak. The high energy fine structure ≥ 5.3 eV is mostly determined by $5d_{\text{O}} \rightarrow t_{2g}$ and $\text{O}_{2p} \rightarrow e_g$ transitions. The spectral features between 8 and 12 eV are due to $5d_{\text{O}} \rightarrow e_g$ transitions. There is relatively large \mathbf{Q} dependence of the RIXS spectrum at the Ir L_3 edge with pronounced periodic modulation of the RIXS intensity as a function of Q_z . In our investigation of the Ir L_3 RIXS spectrum as a function of incident photon energy E_i we found that the low energy fine structure corresponding to the intra- t_{2g} excitation steadily decreases when the incident photon energy changes above the corresponding edge from 11215 to 11220 eV.

The shape of the oxygen K RIXS spectrum at 0–5 eV is very similar to the corresponding RIXS spectrum at the Ir L_3 edge. The two peaks at ≤ 2 eV are derived from the interband transitions between the oxygen $2p$ states

strongly hybridized with the Ir t_{2g} state in close vicinity to the Fermi level. We found that the major contribution to the fine structure situated from 2 to 5 eV is derived from $\text{O}_{2p} \rightarrow \text{O}_{t_{2g}}$ transitions. Opposite to the Ir L_3 RIXS spectrum, the intensity of the oxygen K RIXS spectrum for energies ≥ 5 eV is very large. These structures are derived from $5d_{\text{O}} \rightarrow \text{O}_{t_{2g}}$, $\text{O}_{2p} \rightarrow \text{O}_{e_g}$, and $\text{O}_{t_{2g}} \rightarrow \text{Ba}_{5d}$ transitions.

To investigate the influence of the core state on Nb RIXS spectra, we calculated the RIXS spectra at the Nb K , L_3 , M_3 , M_5 , and N_3 edges. We found a similarity between the Nb K and M_5 RIXS spectra. The major difference is seen from 0 to 7 eV. The difference between the Nb K and M_5 spectra can be attributed to an additional contribution of $4f_{5/2,7/2}$ energy states to the M_5 spectra as well as to the difference in the corresponding radial matrix elements. We found that the RIXS spectra in the row $L_3 - M_3 - N_3$ have almost a similar shape and demonstrate a systematic decrease of intensity. These spectra are more narrow than the K and M_5 RIXS spectra and shifted towards higher energy. This can be explained by a smaller width of the occupied Nb $4d$ states in comparison with the corresponding Nb $5p$ states. Besides, Nb $4d$ states are situated below Nb $5p$ states in energy. The RIXS spectroscopy of Nb atoms at the K , L_3 , M_3 , M_5 , and N_3 edges may be a very useful tool for the investigation of the electronic structure of $\text{Ba}_4\text{NbIr}_3\text{O}_{12}$.

ACKNOWLEDGMENTS

The studies were supported by the National Academy of Sciences of Ukraine within the budget program KP-KBK 6541230 "Support for the development of priority areas of scientific research".

-
- [1] W. Witczak-Krempa, G. Chen, Y. B. Kim, and L. Balents, Correlated quantum phenomena in the strong spin-orbit regime, *Annu. Rev. Condens. Matter Phys.* **5**, 57 (2014).
 - [2] X.-L. Qi and S.-C. Zhang, The quantum spin hall effect and topological insulators, *Physics Today* **63**, 33 (2010).
 - [3] Y. Ando, Topological insulator, *J. Phys. Soc. Jpn.* **82**, 102001 (2013).
 - [4] T. O. Wehling, A. Black-Schafferc, and A. Balatsky, Dirac materials, *Adv. Phys.* **63**, 1 (2014).
 - [5] A. Bansil, L. H, and T. Das, Colloquium: Topological band theory, *Rev. Mod. Phys.* **88**, 021004 (2016).
 - [6] B. J. Kim, H. Jin, S. J. Moon, J.-Y. Kim, B.-G. Park, C. S. Leem, J. Yu, T. W. Noh, C. Kim, S.-J. Oh, J.-H. Park, V. Durairaj, G. Cao, and E. Rotenberg, Novel $j_{\text{eff}}=1/2$ mott state induced by relativistic spin-orbit coupling in Sr_2IrO_4 , *Phys. Rev. Lett.* **101**, 076402 (2008).
 - [7] B. J. Kim, H. Ohsumi, T. Komesu, S. Sakai, T. Morita, H. Takagi, and T. Arima, Phase-sensitive observation of a spin-orbital mott state in Sr_2IrO_4 , *Science* **323**, 1329 (2009).
 - [8] H. Watanabe, T. Shirakawa, and S. Yunoki, Microscopic study of a spin-orbit-induced mott insulator in ir oxides, *Phys. Rev. Lett.* **105**, 216410 (2010).
 - [9] C. Martins, M. Aichhorn, L. Vaugier, and S. Biermann, Reduced effective spin-orbital degeneracy and spin-orbital ordering in paramagnetic transition-metal oxides: Sr_2IrO_4 versus Sr_2RhO_4 , *Phys. Rev. Lett.* **107**, 266404 (2011).
 - [10] W. Witczak-Krempa and Y. B. Kim, Topological and magnetic phases of interacting electrons in the pyrochlore iridates, *Phys. Rev. B* **85**, 045124 (2012).
 - [11] A. Go, W. Witczak-Krempa, G. S. Jeon, K. Park, and Y. B. Kim, Correlation effects on 3d topological phases: From bulk to boundary, *Phys. Rev. Lett.* **109**, 066401 (2012).
 - [12] A. B. Sushkov, J. B. Hofmann, G. S. Jenkins, J. Ishikawa, S. Nakatsuji, S. DasSarma, and H. D. Drew, Optical evidence for a weyl semimetal state in pyrochlore $\text{Eu}_2\text{Ir}_2\text{O}_7$, *Phys. Rev. B* **92**, 241108 (2015).

- [13] I. Kimchi, J. G. Analytis, and A. Vishwanath, Three-dimensional quantum spin liquids in models of harmonic-honeycomb iridates and phase diagram in an infinite-d approximation, *Phys. Rev. B* **90**, 205126 (2014).
- [14] L. Balents, Spin liquids in frustrated magnets, *Nature* **464**, 199 (2010).
- [15] L. Savary and L. Balents, Quantum spin liquids: a review, *Rep. Progr. Phys.* **80**, 016502 (2017).
- [16] D. I. Khomskii, *Transition Metal Compounds* (Cambridge University Press, Cambridge, 2014).
- [17] K. I. Kugel, D. I. Khomskii, A. O. Sboychakov, and S. V. Streltsov, Spin-orbital interaction for face-sharing octahedra: Realization of a highly symmetric $su(4)$ model, *Phys. Rev. B* **91**, 155125 (2015).
- [18] T. Sakamoto, Y. Doi, and Y. Hinatsu, Crystal structures and magnetic properties of 6H-perovskite-type oxides $Ba_3M\text{Ir}2O_9$ ($M=\text{Mg, Ca, Sc, Ti, Zn, Sr, Zr, Cd}$ and In), *J. Solid State Chem.* **179**, 2995 (2006).
- [19] Y. Doi and Y. Hinatsu, The structural and magnetic characterization of 6H-perovskite-type oxides $Ba_3\text{LnIr}2O_9$ ($\text{Ln} = \text{Y, lanthanides}$), *J. Phys.: Condens. Matter* **16**, 2849 (2004).
- [20] T. Dey, A. V. Mahajan, P. Khuntia, M. Baenitz, B. Koteswararao, and F. C. Chou, Spin-liquid behavior in $jeff = 1/2$ triangular lattice compound $Ba_3\text{IrTi}2O_9$, *Phys. Rev. B* **86**, 140405(R) (2012).
- [21] T. Dey, A. V. Mahajan, R. Kumar, B. Koteswararao, F. C. Chou, A. A. Omrani, and H. M. Ronnow, Possible spin-orbit driven spin-liquid ground state in the double perovskite phase of $Ba_3\text{YIr}2O_9$, *Phys. Rev. B* **88**, 134425 (2013).
- [22] T. Dey and A. V. Mahajan, Frustration induced disordered magnetism in $Ba_3\text{RuTi}2O_9$, *Eur. Phys. J. B* **86**, 247 (2013).
- [23] T. Dey, R. Kumar, A. V. Mahajan, S. D. Kaushik, and V. Siruguri, Unconventional magnetism in the spin-orbit-driven mott insulators $Ba_3M\text{Ir}2O_9$ ($M=\text{Sc,Y}$), *Phys. Rev. B* **89**, 205101 (2014).
- [24] A. Nag, S. Middey, S. Bhowal, S. K. Panda, R. Mathieu, J. C. Orain, F. Bert, P. Mendels, P. G. Freeman, M. Mansson, H. Ronnow, M. Telling, P. Biswas, D. Sheptyakov, S. Kaushik, V. Siruguri, C. Meneghini, D. D. Sarma, I. Dasgupta, and S. Ray, Origin of the spin-orbital liquid state in a nearly $J=0$ iridate $Ba_3\text{ZnIr}2O_9$, *Phys. Rev. Lett.* **116**, 097205 (2016).
- [25] R. Kumar, D. Sheptyakov, P. Khuntia, K. Rolfs, P. G. Freeman, H. M. Ronnow, T. Dey, M. Baenitz, and A. V. Mahajan, $Ba_3M_x\text{Ti}_{3-x}O_9$ ($M = \text{Ir, Rh}$): A family of 5d/4d-based diluted quantum spin liquids, *Phys. Rev. B* **94**, 174410 (2016).
- [26] T. Dey, M. Majumder, J. C. Orain, A. Senyshyn, M. Prinz-Zwick, S. Bachus, Y. Tokiwa, F. Bert, P. Khuntia, N. Büttgen, A. A. Tsirlin, and P. Gegenwart, Persistent low-temperature spin dynamics in the mixed-valence iridate $Ba_3\text{InIr}2O_9$, *Phys. Rev. B* **96**, 174411 (2017).
- [27] A. Nag, S. Bhowal, F. Bert, A. D. Hillier, M. Itoh, I. Carlomagno, C. Meneghini, T. Sarkar, R. Mathieu, I. Dasgupta, and S. Ray, $Ba_3M\text{Ir}2O_9$ hexagonal perovskites in the light of spin-orbit coupling and local structural distortions, *Phys. Rev. B* **97**, 064408 (2018).
- [28] M. S. Khan, A. Bandyopadhyay, A. Nag, V. Kumar, A. V. Mahajan, and S. Ray, Magnetic ground state of the distorted 6H perovskite $Ba_3\text{CdIr}2O_9$, *Phys. Rev. B* **100**, 064423 (2019).
- [29] L. T. Nguyen and R. J. Cava, Hexagonal perovskites as quantum materials, *Chem. Rev.* **121**, 2935 (2021).
- [30] C. Garg, A. Cervellino, and S. Nair, Frustration, strain and phase co-existence in the mixed valent hexagonal iridate $Ba_3\text{NaNr}2O_9$, *J. Phys.: Condens. Matter* **34**, 285602 (2022).
- [31] G. Cao, J. Crow, R. Guertin, P. Henning, C. Homes, M. Strongin, D. Basov, and E. Lochner, Charge density wave formation accompanying ferromagnetic ordering in quasi-one-dimensional BaIrO_3 , *Solid State Commun.* **113**, 657 (2000).
- [32] L. T. Nguyen and R. J. Cava, Trimer-based spin liquid candidate $Ba_4\text{NbIr}3O_{12}$, *Phys. Rev. Materials* **3**, 014412 (2019).
- [33] G. Cao, H. Zheng, H. Zhao, Y. Ni, C. A. Pocs, Y. Zhang, F. Ye, C. Hoffmann, X. Wang, M. Lee, M. Hermele, and I. Kimchi, Quantum liquid from strange frustration in the trimer magnet $Ba_4\text{Ir}3O_{10}$, *npj Quantum Mater.* **5**, 26 (2020).
- [34] X. Chen, Y. He, S. Wu, Y. Song, D. Yuan, E. Bourret-Courchesne, J. P. C. Ruff, Z. Islam, A. Fran, and R. J. Birgeneau, Structural and magnetic transitions in the planar antiferromagnet $Ba_4\text{Ir}3O_{10}$, *Phys. Rev. B* **103**, 224420 (2021).
- [35] J. Wilkens and H. Müller-Buschbaum, Zur kenntnis von $Ba_4\text{Ir}_3\text{O}_{10}$, *J. Inorg. Gen. Chem.* **592**, 79 (1991).
- [36] Y. Klein, G. Rousse, F. Damay, F. Porcher, G. Andre, and I. Terasaki, Antiferromagnetic order and consequences on the transport properties of $Ba_4\text{Ru}3O_{10}$, *Phys. Rev. B* **84**, 054439 (2011).
- [37] S. V. Streltsov and D. I. Khomskii, Unconventional magnetism as a consequence of the charge disproportionation and the molecular orbital formation in $Ba_4\text{Ru}3O_{10}$, *Phys. Rev. B* **86**, 064429 (2012).
- [38] G. Cao, H. Zhao, B. Hu, N. Pellatz, D. Reznik, P. Schlottmann, and I. Kimchi, Quest for quantum states via field-altering technology, *npj Quantum Mater.* **5**, 83 (2020).
- [39] Y. Shen, J. Sears, G. Fabbris, A. Weichselbaum, W. Yin, H. Zhao, D. G. Mazzone, H. Miao, M. H. Upton, D. Casa, R. Acevedo-Esteves, C. Nelson, A. M. Barbour, C. Mazzoli, G. Cao, and M. P. M. Dean, Emergence of spinons in layered trimer iridate $Ba_4\text{Ir}3O_{10}$, *Phys. Rev. Lett.* **129**, 207201 (2022).
- [40] A. Bandyopadhyay, S. Lee, D. T. Adroja, M. R. Lees, G. B. G. Stenning, P. Aich, L. Tortora, C. Meneghini, G. Cibirin, A. Berlie, R. A. Saha, D. Takegami, A. Melendez-Sans, G. Poelchen, M. Yoshimura, K. D. Tsuei, Z. Hu, T.-S. Chan, S. Chattopadhyay, G. S. Thakur, and K.-Y. Choi, Gapless dynamic magnetic ground state in the charge-gapped trimer iridate $Ba_4\text{NbIr}3O_{12}$, *Phys. Rev. Mater.* **8**, 074405 (2024).
- [41] Y. Shimoda, Y. Doi, M. Wakeshima, and Y. Hinatsu, Synthesis and magnetic properties of 12l-perovskites $Ba_4\text{LnIr}3O_{12}$ ($\text{Ln} = \text{lanthanides}$), *J. Solid State Chem.* **182**, 2873 (2009).
- [42] Y. Shimoda, Y. Doi, M. Wakeshima, and Y. Hinatsu, Magnetic properties of quadruple perovskites $Ba_4\text{LnRu}3O_{12}$ ($\text{Ln} = \text{La, Nd, Sm-Gd, Dy-Lu}$), *J. Solid State Chem.* **183**, 33 (2010).
- [43] K. E. Stitzer, M. D. Smith, and H.-C. zur Loye, Crystal growth, structure determination and magnetic properties of $Ba_4\text{Ir}3O_{10}$ and $Ba_4(\text{Co}_0.4\text{Ir}_0.6)\text{Ir}2O_{10}$, *J. Appl.*

- Crystallogr. **338**, 104 (2002).
- [44] R. W. Wyckoff, *Crystal Structures* (Wiley, New York, 1963).
- [45] H. k. Müller-Buschbaum and C. Lang, Ba₅AlIr₂O₁₁: Eine neue Verbindung mit Iridium(IV, V), *Z. Anorg. Allg. Chem.* **568**, 29 (1989).
- [46] L. T. Nguyen, T. Halloran, W. Xie, T. Kong, C. L. Broholm, and R. J. Cava, Geometrically frustrated trimer-based Mott insulator, *Phys. Rev. Mater.* **2**, 054414 (2018).
- [47] G. S. Thakur, S. Chattopadhyay, T. H. T. Doert, and C. Felser, Crystal growth of spin-frustrated Ba₄Nb_{0.8}Ir_{3.2}O₁₂: A possible spin liquid material, *Cryst. Growth Des.* **20**, 2871 (2020).
- [48] E. V. Komleva, D. I. Khomskii, and S. V. Streltsov, Three-site transition-metal clusters: Going from localized electrons to molecular orbitals, *Phys. Rev. B* **102**, 174448 (2020).
- [49] L. J. P. Ament, M. van Veenendaal, T. P. Devereaux, J. P. Hill, and J. van den Brink, Resonant inelastic x-ray scattering studies of elementary excitations, *Rev. Mod. Phys.* **83**, 705 (2011).
- [50] F. M. F. de Groot, M. W. Haverkort, H. Elnaggar, A. Juhin, K.-J. Zhou, and P. Glatzel, Resonant inelastic x-ray scattering, *Nat. Rev. Methods Primers* **4**, 46 (2024).
- [51] M. Magnaterra, A. Sandberg, H. Schilling, P. Warzanowski, L. Pätzold, E. Bergamasco, C. J. Sahle, Detlefs, K. Ruotsalainen, M. M. Sala, G. Monaco, P. Becker, Q. Faure, G. S. Thakur, , M. Songvilay, C. Felser, P. H. M. van Loosdrecht, J. van den Brink, M. Hermanns, and M. Grüninger, Quasimolecular electronic structure of the trimer iridate Ba₄NbIr₃O₁₂, *Phys. Rev. B* **111**, 085122 (2025).
- [52] V. V. Nemoshkalenko, A. E. Krasovskii, V. N. Antonov, V. N. Antonov, U. Fleck, H. Wonn, and P. Ziesche, The relativistic linear muffin-tin orbital method. application to Au, *Phys. status solidi B* **120**, 283 (1983).
- [53] E. Arola, P. Strange, and B. L. Gyroffly, Relativistic theory of magnetic scattering of x rays: Application to ferromagnetic iron, *Phys. Rev. B* **55**, 472 (1997).
- [54] V. N. Antonov, D. A. Kukusta, and L. V. Bekenov, Electronic structure and resonant inelastic x-ray scattering in the osmates: I. perovskite NaOsO₃, *Phys. Rev. B* **105**, 155144 (2022).
- [55] V. N. Antonov, O. Jepsen, A. N. Yaresko, and A. P. Shpak, Electronic structure and x-ray magnetic circular dichroism in the Heusler alloy Co₂MnGe, *J. Appl. Phys.* **100**, 043711 (2006).
- [56] V. N. Antonov, B. N. Harmon, A. N. Yaresko, and A. P. Shpak, X-ray magnetic circular dichroism in the GdN: First-principles calculations, *Phys. Rev. B* **75**, 184422 (2007).
- [57] V. N. Antonov, A. N. Yaresko, and O. Jepsen, X-ray magnetic dichroism in the III–V diluted magnetic semiconductors: First principle calculations, *Phys. Rev. B* **81**, 075209 (2010).
- [58] O. K. Andersen, Linear methods in band theory, *Phys. Rev. B* **12**, 3060 (1975).
- [59] V. Antonov, B. Harmon, and A. Yaresko, *Electronic Structure and Magneto-Optical Properties of Solids* (Kluwer, Dordrecht, 2004).
- [60] J. P. Perdew, K. Burke, and M. Ernzerhof, Generalized gradient approximation made simple, *Phys. Rev. Lett.* **77**, 3865 (1996).
- [61] P. E. Blöchl, O. Jepsen, and O. K. Andersen, Improved tetrahedron method for Brillouin-zone integrations, *Phys. Rev. B* **49**, 16223 (1994).
- [62] V. N. Antonov, D. A. Kukusta, and L. V. Bekenov, Electronic structure and resonant inelastic x-ray scattering in the osmates: II. pyrochlore Cd₂Os₂O₇, *Phys. Rev. B* **105**, 155145 (2022).
- [63] J. P. Perdew and A. Zunger, Self-interaction correction to density-functional approximations for many-electron systems, *Phys. Rev. B* **23**, 5048 (1981).
- [64] H. Lin, R. S. Markiewicz, L. A. Wray, L. Fu, M. Z. Hasan, and A. Bansil, Single-dirac-cone topological surface states in TlBiSe₂ class of topological insulators, *Phys. Rev. Lett.* **105**, 036404 (2010).
- [65] T. Kaneko, T. Toriyama, T. Konishi, and Y. Ohta, Orthorhombic-to-monoclinic phase transition of Ta₂NiSe₅ induced by the Bose-Einstein condensation of excitons, *Phys. Rev. B* **87**, 035121 (2013).
- [66] T. I. Larkin, A. N. Yaresko, D. Pröpper, K. A. Kikoin, Y. F. Lu, T. Takayama, Y.-L. Mathis, A. W. Rost, H. Takagi, B. Keimer, and A. V. Boris, Giant exciton Fano resonance in quasi-one-dimensional Ta₂NiSe₅, *Phys. Rev. B* **95**, 195144 (2017).
- [67] D. A. Kukusta, L. V. Bekenov, A. N. Yaresko, K. Ishii, T. Takayama, H. Takagi, and N. Antonov, Electronic structure and resonant inelastic x-ray scattering in Ta₂NiSe₅, *J. Phys.: Condens. Matter* **27**, 255501 (2025).
- [68] G. van der Laan and B. T. Thole, Local probe for spin-orbit interaction, *Phys. Rev. Lett.* **60**, 1977 (1988).
- [69] V. N. Antonov, D. A. Kukusta, and L. V. Bekenov, Electronic structure and resonant inelastic x-ray scattering in the mixed 3d-5d transition-metal oxides Sr₃CuIrO₆, Sr₃CuPtO₆, and Sr₃ZnIrO₆, *J. Electron. Spectrosc. Relat. Phenom.* **270**, 147416 (2024).
- [70] D. Haskel, G. Fabbris, M. Zhernenkov, P. P. Kong, C. Q. Jin, G. Cao, and M. van Veenendaal, Pressure tuning of the spin-orbit coupled ground state in Sr₂IrO₄, *Phys. Rev. Lett.* **109**, 027204 (2012).
- [71] M. Ye, H.-S. Kim, J.-W. Kim, C.-J. Won, K. H. Aand D. Vanderbilt, S.-W. Cheong, and G. Blumberg, Covalency-driven collapse of strong spin-orbit coupling in face-sharing iridium octahedra, *Phys. Rev. B* **98**, 201105(R) (2018).
- [72] A. Nag, S. Bhowal, M. M. Sala, A. Efimenko, I. Dasgupta, and S. Ray, Hopping-induced ground-state magnetism in 6H perovskite iridates, *Phys. Rev. Lett.* **123**, 017201 (2019).
- [73] Y. Wang, R. Wang, J. Kim, M. H. Upton, D. Casa, T. Gog, G. Cao, G. Kotliar, M. P. M. Dean, and X. Liu, Direct detection of dimer orbitals in Ba₅AlIr₂O₁₁, *Phys. Rev. Lett.* **122**, 106401 (2019).
- [74] A. Revelli, M. M. Sala, G. Monaco, M. Magnaterra, J. Attig, L. Peterlini, T. Dey, A. A. T. and P. Gegenwart, T. Fröhlich, M. Braden, C. Grams, J. Hemberger, P. Becker, P. H. M. van Loosdrecht, D. I. Khomskii, J. van den Brink, M. Hermanns, and M. Grüninger, Quasimolecular electronic structure of the spin-liquid candidate Ba₃InIr₂O₉, *Phys. Rev. B* **106**, 155107 (2022).
- [75] V. N. Antonov, S. Uba, and L. Uba, Electronic structure and x-ray magnetic circular dichroism in the hyperhoneycomb iridate beta-Li₂IrO₃, *Phys. Rev. B* **98**, 245113 (2018).

- [76] T. Takayama, A. Krajewska, A. S. Gibbs, A. N. Yaresko, H. Ishii, H. Yamaoka, K. Ishii, N. Hiraoka, N. P. Funnell, C. L. Bull, and H. Takagi, Pressure-induced collapse of spin-orbital mott state in the hyperhoneycomb iridate beta-Li₂IrO₃, *Phys. Rev. B* **99**, 125127 (2019).
- [77] V. N. Antonov, D. A. Kukusta, L. Uba, A. Bonda, and S. Uba, Resonant inelastic x-ray scattering spectra in the hyperhoneycomb iridate beta-Li₂IrO₃: First-principles calculations, *Phys. Rev. B* **103**, 235127 (2021).
- [78] X. Liu, V. M. Katukuri, L. Hozoi, W.-G. Yin, M. P. M. Dean, M. H. Upton, J. Kim, D. Casa, A. Said, T. Gog, T. F. Qi, G. Cao, A. M. Tsvelik, J. van den Brink, and J. P. Hill, Testing the validity of the strong spin-orbit-coupling limit for octahedrally coordinated iridate compounds in a model system Sr₃CuIrO₆, *Phys. Rev. Lett.* **109**, 157401 (2012).
- [79] A. Krajewska, T. Takayama, R. Dinnebier, A. Yaresko, K. Ishii, M. Isobe, and H. Takagi, Almost pure $j_{\text{eff}} = 1/2$ mott state of In₂Ir₂O₇ in the limit of reduced intersite hopping, *Phys. Rev. B* **101**, 121101(R) (2020).
- [80] A. Revelli, M. M. Sala, G. Monaco, P. Becker, L. Bohaty, M. Hermanns, T. C. Koethe, T. Fröhlich, P. Warzanowski, T. Lorenz, S. V. Streltsov, P. H. M. van Loosdrecht, D. I. Khomskii, J. van den Brink, and M. Grüninger, Resonant inelastic x-ray incarnation of young's double-slit experiment, *Sci. Adv.* **5**, eaav4020 (2019).
- [81] M. Magnaterra, J. Attig, L. Peterlini, M. Hermanns, M. H. Upton, J. Kim, L. Prodan, V. Tsurkan, I. Kezsmarki, P. H. M. van Loosdrecht, and M. Grüninger, Quasimolecular $j_{\text{tet}} = 3/2$ moments in the cluster mott insulator GaTa₄Se₈, *Phys. Rev. Lett.* **133**, 046501 (2024).
- [82] H. Ebert, Fully relativistic treatment of core states for spin-dependent potential, *J. Phys.: Condens. Matter* **1**, 9111 (1989).